Theoretical description of fast kinetic electron emission in ion-surface collisions

Carlos O. Reinhold and Joachim Burgdörfer
Physics Division, Oak Ridge National Laboratory, Oak Ridge, Tennessee 37831-6373
and University of Tennessee, Knoxville, Tennessee 37996-1200
(Received 3 July 1996)

We present a microscopic description of the emission of fast electrons in glancing-angle ion-surface collisions. We employ a classical trajectory Monte Carlo approach that treats the primary production of kinetic electrons in close collisions and their subsequent transport through the surface region on the same footing. Dynamic image interactions and multiple scattering are explicitly included. As an application, we analyze the ejected electron spectra over a broad range of electron energies and emission angles for 0.2–0.5-MeV/u Li ions interacting with SnTe(001) surfaces. Good agreement is found with experiment for the shape of the spectrum of forward-ejected electrons containing prominent structures such as the convoy electron peak and the binary ridge. [S1050-2947(97)02201-4]

PACS number(s): 79.20.Rf, 34.50.Fa

I. INTRODUCTION

The study of kinetic electron emission in ion-solid collisions provides an important link between atomic physics and condensed matter physics. Comparative analysis of spectra from ion-atom, ion-solid (transmission), and ion-surface (glancing incidence) collisions affords the opportunity to extract detailed information about long-ranged image interactions and multiple scattering in the solid and near the surface.

The so-called convoy electron peak (CEP) represents an illuminating example for such differences. This peak was experimentally discovered two decades ago as a cusp-shaped structure in the spectra of electrons arising from ion-atom [1] and ion-solid (transmission) collisions [2] for electrons ejected with velocities $\vec{v}_e$ close to the projectile velocity $\vec{v}_p$. Because cusp electrons recede from the target in close spatial correlation with the projectile, the behavior of the cross sections in the limit $|\vec{v}_e-\vec{v}_p|\to 0$ was found to be governed by threshold laws characteristic of the two-body final-state interaction between the electron and the projectile. The existence of similar peaks in ion-atom and ion-solid collisions is simply a consequence of the fact that the final-state two-body interaction is identical. Analysis of the detailed shape of the CEP for ion-atom and ion-solid collisions has revealed, however, that the dynamics responsible for the population of low-lying continuum states is vastly different. In particular, the dynamics for ion-solid collisions is characterized by a complex array of multiple scattering events that can lead to the population of large angular momentum states (see, e.g., [3–5] and references therein).

Recent experiments concerning glancing-angle ion-surface interactions have revealed a prominent structure at forward ejection angles near the region where the CEP is expected to appear in foil transmission experiments [6–13]. Compared to the peak for transmission conditions, however, the convoy peak for ion-surface collisions is dramatically broadened and shifted in energy. The first evidence for broadening of the CEP was found by DeFerraris and Baragiola [6] for scattering of protons at an Al surface. A similar broadening was observed for semiconductor surfaces [7,8]. Concurrently, a shift of the CEP to electron velocities larger than v_p was proposed [9] and independently measured [7] for projectile charges greater than one. Subsequently, large shifts of up to 100 eV have been observed in several laboratories and a number of explanations have been proposed [9–16].

The theoretical description of fast electron emission in glancing-angle ion-surface scattering is still in its infancy. Iitaka *et al.* [15] and Kimura *et al.* [12] have shown a classical trajectory Monte Carlo (CTMC) simulation using an ensemble of initial conditions from a simple model (electrons distributed in a shell around the projectile) rather than a microscopic theory. Taking into account the propagation of the electrons in the combined field of the projectile and its image, they found a shift of the CEP. First-order Born approximation calculations have been performed for electron emission by resonant coherent excitation (RCE) [17] and for the emission from a jelliumlike conduction band [18]. Within a perturbative approach, however, dynamic image potential effects on the final state and multiple scattering are difficult to incorporate. Moreover, for multiply charged ions and intermediate velocities perturbation theory breaks down.

In the following, we present a comprehensive CTMC description of kinetic electron emission. Its major approximation consists of a classical description of the motion of the ejected electron. To date, the CTMC method has proven to be one of the most successful approximations in describing absolute ejected electron spectra at intermediate energy atomic collisions (i.e., ion velocities similar to initial orbital velocities of electrons in the target) [19]. The approximate validity of the classical description can be theoretically justified based on the observation that for collision processes at intermediate velocities large momentum transfers dominate and quantum corrections are, on the average, small [20].

The present theory is a combination of the CTMC method as applied to atomic collisions [19,21] and the classical transport theory originally developed for transmission of ions or atoms through solids [22]. Accordingly, the initial close collisions between the projectile ion and electrons of the target and the subsequent transport through the surface region and out to asymptotic distances is treated on the same foot-

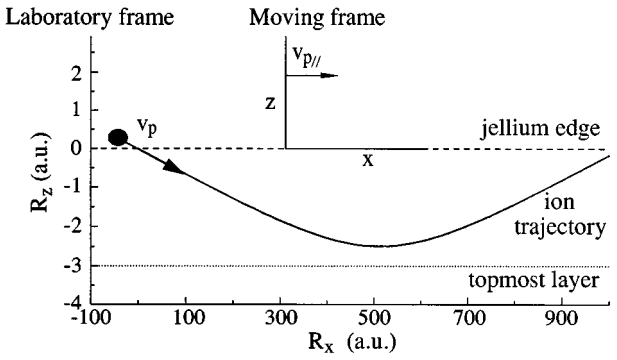

FIG. 1. Coordinate systems and ion trajectory for a 0.3-MeV/u Li^{1+}-SnTe collision.

ing. This approach permits the nonpertubative treatment of the core potentials and long-range dynamic image potentials as well as the incorporation of multiple-scattering-induced energy loss and straggling effects. A preliminary account with an application to the CEP peak was given in [23]. In the present work we give a more detailed outline of the theoretical framework and apply it to the emission spectrum of electrons in $Li^{q+} \rightarrow$SnTe collisions for a broad range of emission angles and energies.

In order to improve the clarity of presentation, we defer some of the technical aspects to the Appendices. Atomic units are used throughout unless otherwise stated.

II. THEORY

We shall be concerned with the scattering of a heavy ion with nuclear charge Z_p, ionic charge Q_p, mass M_p, and initial velocity $\vec{v}_p$ at an ideally flat surface at grazing incidence. All numerical calculations throughout this paper will refer to a SnTe(100) surface. However, the method is, with minor modifications, applicable to other semiconductor or metal surfaces. The projectile is assumed to be fast compared to the Fermi velocity v_F of the crystal ($v_p > 2v_F$), which corresponds to impact energies in the range of hundreds of keV/u. We shall assume that the incidence angle of the ion with respect to the surface θ_p is small enough so that the ion is specularly reflected (a value $\theta_p = 6$ mrad will be used throughout, which corresponds to the experimental value of Kimura *et al.* [12,24]). We neglect the slowing down of the heavy ion due to its interaction with the surface. Typical energy losses are less than 3% of the incident energy (e.g., [25]), which has a negligible effect in the evolution of fast electrons. Thus, the velocity of the ion parallel to the surface, $\vec{v}_{p_\parallel} = v_p \cos\theta_p \hat{x}$ is a constant of motion in a grazing collision under surface channeling conditions.

The position vector and momentum of the impinging ion in the laboratory frame shall be denoted by $\vec{R} = (v_{p_\parallel} t, 0, R_z(t))$ and $\vec{P} = (M_p v_{p_\parallel}, 0, P_z(t))$, respectively. The surface is in the (x,y) plane and the projectile is moving in the direction of the positive x axis (see Fig. 1). Similarly, $\vec{r}$ and $\vec{p}$ are used to denote the position vector and the momentum of an electron in the laboratory frame [in atomic units $\vec{p} = \vec{v_e} = (v_x, v_y, v_z)$, v_e being the velocity of the electron]. The origin is at the jellium edge, which is displaced from the topmost atomic layer by z_J, corresponding to one-half of the nearest-neighbor distance ($z_J = 2.99$ a.u. for SnTe [26]). We note, however, that our description of the surface incorporates features beyond the jellium model. Specifically, the effect of the ionic core and the core electron density will be explicitly taken into account. Alternatively, we will adopt the moving coordinate system of Fig. 1. The position of an electron in the moving frame is denoted by $\vec{s} = (x,y,z) = \vec{r} - v_{\vec{p}_\parallel} t$.

A. Hamiltonian

Within the framework outlined above, the effective Hamiltonian describing the ion-surface interaction is given by

$$H = H_p(\vec{R}) + \sum_{j=1}^{N_e} H_e(\vec{r}_j, \vec{R}), \tag{1}$$

where H_p denotes the Hamiltonian for the projectile motion while H_e represents the Hamiltonian of the jth active electron treated in the independent electron approximation. The total number of active electrons is given by N_e. The Hamiltonian functions in Eq. (1) are of the form

$$H_p(\vec{R}) = \frac{P^2}{2M_p} + V_p(\vec{R}) \tag{2}$$

and

$$H_e(\vec{r},\vec{R},t) = H_0^i(\vec{r},\vec{p},t) + V(\vec{r},t) - \vec{r}\cdot\vec{F}_{\rm st}(t) \tag{3}$$

In Eq. (2), $V_p(\vec{R})$ is the effective potential experienced by the projectile along the trajectory. The electronic Hamiltonian H_e contains, in addition to the channel Hamiltonian H_0^i, which defines the unperturbed initial state of the electron, a perturbation potential $V(\vec{r},t)$ as well as energy loss and straggling through a stochastic force $F_{\rm st}$ describing inelastic and elastic collisions in the vicinity of the surface. Elastic collisions represent elastic scattering of the electron at the screened heavy nuclei in the solid. Inelastic collisions consist of single-particle–single-hole and plasmon excitations of valence electrons. Electron-electron interactions are only accounted for through dynamic image interactions, static atomic screening, and collision kernels.

The fundamental assumption underlying Eq. (2) is the decoupling of the dynamics of the impinging ion from the electronic dynamics. An approximate ionic trajectory is determined by V_p. Subsequently, electrons are assumed to evolve according to a time-dependent Hamiltonian containing the trajectory $\vec{R}(t)$ of the projectile. The different microscopic interactions that govern the ionic and electronic dynamics will be discussed in more detail below. The assumption of the decoupling of ionic and electronic degrees of freedom appears justified for fast collisions because of the disparity between the energies of the electronic and ionic motion. As will be discussed below, this condition is not quite sufficient as the energy of the perpendicular motion of the ion is small in grazing collisions. In addition, the rapid fluctuations of the charge state of the ion during the extended interaction time

are a prerequisite for establishing a mean-field potential for the ion and, hence, for the validity of the decoupling.

B. Monte Carlo solution of the classical Liouville equation

The electronic time-dependent evolution can be represented by a phase-space number density of electrons, $\aleph(\vec{r},\vec{p},t)$. Initially,

$$\aleph(\vec{r},\vec{p},t=-\infty)=\sum_{i=1}^{N_\chi} g_{\chi_i} f_{\chi_i}(\vec{r},\vec{p},t=-\infty), \tag{4}$$

where the sum extends over all occupied and ''active'' orbitals χ_i with multiplicities g_{χ_i} ($\Sigma_{i=1}^{N\chi} g_{\chi_i}=N_e$). In Eq. (4) f_{χ_i} denotes the classical phase-space representation of the orbital χ_i defined in terms of the effective single-particle channel Hamiltonian H_0^i such that

$$\int d^3r \int d^3p f_{\chi_i}(\vec{r},\vec{p},t)=1. \tag{5}$$

Formally, the time evolution of $\aleph(\vec{r},\vec{p},t)$ is generated by the classical time-dependent Liouville equation with the Hamiltonian $H_e(\vec{r},\vec{p},t)$. The absolute differential yield Y of ejected electrons per incoming ion can be obtained from the $t\to\infty$ limit of $\aleph$ as

$$\frac{d^3Y}{dp^3}=\lim_{t\to\infty}\int_{\mathfrak{R}} d^3r\aleph(\vec{r},\vec{p},t) \tag{6}$$

where the integration domain $\mathfrak{R}$ corresponds to escaping electrons (i.e., electrons with $z>0$, $p_z>0$ and with positive binding energy with respect to both the target and the projectile).

The CTMC method corresponds to a Monte Carlo solution of the Liouville equation in terms of an ensemble of representative test particles that have propagated according to the stochastic equation of motion (i.e., a Langevin equation) generated by H_e:

$$\frac{d\vec{r}}{dt}=\vec{p}, \quad \frac{d\vec{p}}{dt}=-\vec{\nabla}H_0^i-\vec{\nabla}V+\vec{F}_{\rm st}. \tag{7}$$

In the derivation of this Langevin equation from the Hamiltonian [Eq. (3)], the implicit velocity dependence of the interaction with the environment (''heat bath'') is not treated as a canonical variable of the subsystem.

In order to fix the number of active electrons N_e entering the CTMC simulation, we choose a rectangular volume with side lengths Δx, Δy, and Δz, which is centered at the point of closest approach. Typically, these lengths are $\Delta x\sim 1200$ a.u., $\Delta y\sim 7$ a.u., and $\Delta z\sim 6$ a.u. Consequently, the total number of ''active'' electrons in our simulation, N_e, is given by the sum of all active projectile electrons, N_p, target valence electrons, N_t^v, and target core electrons, N_t^c:

$$N_e=N_p+N_t^v+N_t^c, \tag{8}$$

with

$$N_t^v=n_v\Delta x\Delta y\Delta z, \tag{9}$$

$$N_t^c=N_t^{\rm at}n_s^{\rm at}\Delta x\Delta y, \tag{10}$$

where n_v is the volume number density of valence electrons, $n_s^{\rm at}$ is the areal number density of surface atoms, and $N_t^{\rm at}$ is the total number of active electrons in a single target core.

The Monte Carlo solution of the Liouville equation consists of three steps: (i) a large ensemble of phase-space points $N_{\rm traj}$ is chosen at $t=t_0$ ($t_0\to-\infty$) to simulate $\aleph(\vec{r},\vec{p},t_0)$, (ii) the independent evolution of each phase-space point is calculated up to a final time t_f ($t_f\to\infty$) by numerically integrating the Langevin equations of motion [Eq. (7)], and (iii) the final-state distribution of the electron is determined by binning the phase points at $t=t_f$. In order to achieve sufficient statistical accuracy, a large number of trajectories $N_{\rm traj}\sim 5\times 10^7$ is computed. Denoting $N(\Omega,\Delta\Omega,E,\Delta E)$ the number of electrons found in the bin delimited by the solid angle interval $(\Omega-\Delta\Omega/2,\Omega+\Delta\Omega/2)$ and energy interval $(E-\Delta E/2,E+\Delta E/2)$, the yield of outgoing electrons per ion, solid angle, and energy is given by

$$\frac{d^3Y}{dEd\Omega}=N_e\frac{N(\Omega,\Delta\Omega,E,\Delta E)}{N_{\rm traj}\Delta E\Delta\Omega}. \tag{11}$$

The statistical uncertainty of this yield is approximately given by $1/\sqrt{N(\Omega,\Delta\Omega,E,\Delta E)}$ and we require it to be smaller than $\sim 10\%$.

In this work we only include the primary electrons that are produced by a hard encounter with the impinging ion. We neglect the shower of secondary electrons arising from collisions of primary electrons with other electrons in the solid, which is the dominant mechanism for the production of soft electrons. Thus, we follow the time evolution only of electrons with large enough kinetic energy ($E>v_p^2/4$). The integration is stopped when the kinetic energy of the electron in all degrees of freedom is conserved as a function of time. For free electrons inside the solid the integration is stopped if their depth is larger than ten inelastic mean free paths or after they have been slowed down to energies $E<v_p^2/4$.

III. INTERACTION POTENTIALS

The simulation outlined above requires the specification of several interaction potentials. In this section we discuss our choices for the present collision system. Some of the technical details will be given in the Appendices. We emphasize that application of the theoretical framework to other surfaces and projectiles only requires changes in the input potentials discussed in this section.

A. Projectile potential

The effective projectile potential V_p [Eq. (2)] governing the trajectory of the impinging ion is given under surface channeling conditions by

$$V_p(\vec{R})=V_{\rm planar}^M(R_z)+V_p^{\rm SI}(\vec{v}_{p_\parallel},R_z), \tag{12}$$

which is only dependent on the surface normal coordinate R_z. In Eq. (12), the planar averaged Moliere potential is given by

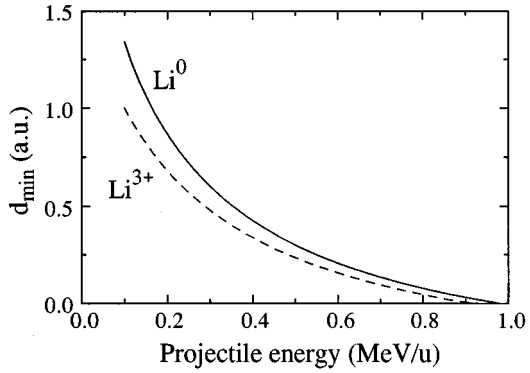

FIG. 2. Distance of closest approach to the topmost target layer, $d_{\min}$, as a function of the collision energy for Li^{Q_p+} ions incident on a SnTe surface with an angle $\theta_p=6$ mrad, calculated for a fixed ionic charge.

$$V^M_{\text{planar}}(R_z)=2\pi n_s^{\text{at}} Z_p Z_t a_t \sum_{k=1}^{3} \frac{c_k}{d_k} e^{-d_k(R_z+z_J)/a_t}, \quad (13)$$

where we have used the Moliere parameters [27] ($c_k=0.35,0.55,0.1$; $d_k=0.3,1.2,6$) with the Thomas-Fermi screening parameter $a_t=0.885(Z_p^{1/2}+Z_t^{1/2})^{-2/3}$. Because of the very similar values of the nuclear charges of Sn and Te atoms ($Z_{\text{Sn}}=50$ and $Z_{\text{Te}}=52$), the planar potential can be approximated for all practical purposes by the one associated with a single atomic charge number $Z_t=(Z_{\text{Sn}}+Z_{\text{Te}})/2=51$ and surface density $n_s^{\text{at}}=1/(4z_J^2)$.

In addition to the planar Moliere potential, the charged ion interacts with its own image through the self-image (SI) potential $V_p^{\text{SI}}(\vec{v}_{p\parallel},R_z)$. The latter can be expressed in terms of the dynamic screening potential as

$$V_p^{\text{SI}}(\vec{v}_{p\parallel},R_z)=\frac{Q_p^2}{2}V^I(\vec{v}_{p\parallel},R_z,\hat{z}R_z) \quad (14)$$

whose calculation is described in Appendix A. The potential V_p^{SI} plays an important role for the image acceleration of the ion toward the surface [28].

A typical ion trajectory is depicted in Fig. 1. Collisions leading to ionization and charge exchange are quite sensitive to the distance of closest approach to the topmost layer, $d_{\min}=(R_z^{\min}+z_J)$, which is determined by the conservation of energy for the perpendicular motion

$$V^M_{\text{planar}}(R_z^{\min})+V_p^{\text{SI}}(\vec{v}_{p\parallel},R_z^{\min})=\tfrac{1}{2}M_p(v_p\sin\theta_p)^2=E_\perp . \quad (15)$$

This distance determines which target and projectile shells are active participants in the collision. For example, Fig. 2 indicates that for the angles of incidence and collision energies of interest in this work, Li ions are found to easily penetrate the core ($d_{\min}<1.5$ a.u.). Consequently, the core level contribution to excitation, ionization, and charge transfer must be included. The image acceleration of the impinging ion (absent for neutral projectiles) becomes increasingly important for small perpendicular collision energies ($E_\perp<$ 100 eV).

B. Electronic channel potentials and initial microcanonical distribution functions

The electronic interaction potentials entering the channel Hamiltonian H_0^i [Eq. (3)] depends on the initial state χ_i. Electrons in the valence band of SnTe are treated as a free-electron gas with volume number density n_v and energy density of states $D(E)\propto\sqrt{E-V_0}$, where $0<E-V_0<\epsilon_F=(3\pi^2 n_v)^{2/3}/2$ and V_0 is the bottom of the valence band. The valence band of the SnTe crystal is derived from the outermost isolated-atom electronic configurations $\mathrm{Sn}(5s^2,5p^2)$ and $\mathrm{Te}(5s^2,5p^4)$. This yields $n_v=5/(8z_J^3)=0.0233$ a.u. and $\epsilon_F=0.391$ a.u., which are very similar to the values $n_v=0.0245$ a.u., $\epsilon_F=0.404$ a.u. obtained from the main plasmon frequency ($\omega_p^2=4\pi n_v$) in photoabsorption measurements [26].

Accordingly, the corresponding channel potential V_t^v is given by the static surface barrier potential V_b. In this work we make use of the static potential barrier parametrized by Jennings *et al.* [29] as a function of the Wigner-Seitz radius, $r_S=[3/(4\pi n_v)]^{1/3}$,

$$V_t^v(z)=V_b(z)=\begin{cases}\dfrac{-1}{4\tilde{z}}(1-e^{-b_1\tilde{z}}) & \text{if } \tilde{z}\geqslant 0\\[2ex] \dfrac{-V_0}{ae^{b_2\tilde{z}}+1} & \text{if } \tilde{z}<0,\end{cases} \quad (16)$$

where $\tilde{z}=z-z_{\text{im}}$, z_{im} is the position of the image plane and the height of the potential barrier, $V_0=\epsilon_F+W$, with W being the work function. For SnTe we use the following parameter values: $W=0.165$ a.u., $V_0=0.569$ a.u., $r_S=2.135$ a.u., $z_{\text{im}}=0.697$ a.u., $a=0.88$, $b_1=1.21$ a.u., and $b_2=1.29$ a.u.

With the help of the channel potential V_t^v we represent the initial phase-space density of valence electrons by

$$f_v^{(t)}(\vec{r},\vec{p})=C_v\Theta\left[-W-\frac{p^2}{2}-V_t^v(z)\right], \quad (17)$$

where C_v is a normalization constant and Θ is a step function. In the bulk limit ($z\to-\infty$), Eq. (17) reproduces the correct density of states of a free-electron gas. Moreover, the local density as a function of z [i.e., integrating $f_v^{(t)}(\vec{r},\vec{p})$ over $\vec{p},x$, and y] is directly proportional to $[-W-V_t^v(z)]^{3/2}$ and is found to approximate the density calculated by Lang and Kohn [30] in the local density approximation (LDA) for $r_S=2$ a.u. remarkably well (Fig. 3). The main differences between the classical and the quantum results are that (i) the quantum density exhibits Friedel oscillations (fairly weak for $r_S=2$ a.u.) and (ii) the classical density has a sharp cutoff at $z=1.823$ a.u. given by the classical turning point of electrons at the Fermi edge (i.e., $\epsilon_F=V_b$) rather than a decreasing tail.

We treat core electrons below the valence band of SnTe as well as localized atomiclike orbitals with quantum numbers n,ℓ. The core potential V_t^c supporting these orbitals has the form of a muffin-tin potential derived from atomic core potentials V^{at},

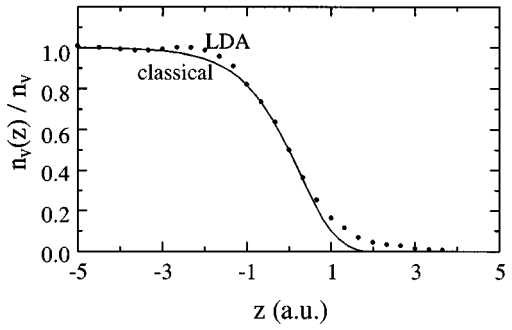

FIG. 3. Density of valence electrons near the surface barrier as a function of the position of the electron, z, with respect to the jellium edge. LDA calculations for $r_S=2$ a.u. from Ref. [30].

$$V_t^c(r)=\min\{[V^{\rm at}(|\vec{r}-\vec{R}_t|)+V^{\rm screen}(|\vec{r}-\vec{R}_t|)],V_b(z)\}, \tag{18}$$

where R_t is the position of a target nucleus and $V^{\rm screen}(r)=[1-\exp(-r/r_0)]/r$ is incorporated to remove the long-range $\sim -1/r$ tail of the atomic potential at large distances. $V^{\rm at}$ is calculated using the two-parameter Hartree-Fock ionic core potentials tabulated by Garvey *et al.* [31].

Using Eq. (18), the initial phase-space distribution function for core electrons can be calculated from a restricted microcanonical distribution [19]:

$$f_{\rm nl}^{(t)}(\vec{r},\vec{p})=C_{\rm nl}\delta\left[\frac{p^2}{2}+V_t^c(|\vec{r}-\vec{R}_t|)-E_{\rm nl}\right] \times\Theta(l_c-l)\Theta(l+1-l_c), \tag{19}$$

where $C_{\rm nl}$ is a normalization constant. In Eq. (19) we have imposed the restriction $\Theta(l_c-l)\Theta(l+1-l_c)$ on the scaled classical angular momentum, $l_c=|(\vec{r}-\vec{R}_t)\times\vec{p}|(n/l_{\rm max})$, such that the subset of the microcanonical ensemble lies in the proper l_c bin associated with the quantum number of the orbital. The binding energies $E_{\rm nl}$ entering Eq. (19) are calculated by numerically solving the radial Schrödinger equation associated with V_t^c. The resulting energies are shown in Table I for the relevant $4d$, $4p$, and $4s$ orbitals in our simulation. A value $r_0=3$ a.u. in Eq. (18) has been chosen, which yields good agreement between the calculated and measured [32] $4d$ energy levels of SnTe. As expected, energy levels of core electrons in the solid are very similar to orbital energy levels of isolated atoms.

States of electrons initially bound to the impinging ion could be easily modeled by phase-space distributions analogous to Eq. (19) using the appropriate orbital energies and core potentials V_p^c of isolated ions. These electrons will not be considered in the following. As discussed below, they are expected to give a negligible contribution to the yield of electrons for the collision system under consideration.

TABLE I. Orbital energies, $E_{\rm nl}$, average linear, $\langle v\rangle_{\rm nl}$, and quadratic, $\sqrt{\langle v^2\rangle_{\rm nl}}$ velocities, and average radius, $\langle r\rangle_{\rm nl}$ in atomic units.

Orbital	$-E_{\rm nl}$	$\langle v\rangle_{\rm nl}$	$\sqrt{\langle v^2\rangle_{\rm nl}}$	$\langle r\rangle_{\rm nl}$
Sn($4d^{10}$)	0.977	3.65	4.88	1.080
Te($4d^{10}$)	1.648	4.12	5.47	0.961
Sn($4p^6$)	3.196	3.71	5.82	0.902
Te($4p^6$)	4.163	4.06	6.32	0.835
Sn($4s^2$)	4.390	3.39	6.17	0.850
Te($4s^2$)	5.485	3.69	6.66	0.794

C. Perturbation potential

The perturbation potential $V(\vec{r},t)$ entering H_e [Eq. (3)] is given by

$$V(\vec{r},t)=V_p^c[|\vec{r}-\vec{R}(t)|]+V_{pe}^I[\vec{r},R_z(t)]+\Delta V_b(v_e,z), \tag{20}$$

where V_p^c is the core potential of the impinging projectile and V_{pe}^I is the image potential induced by the projectile and ΔV_b is a velocity-dependent condition to the barrier potential. V_p^c for dressed ions is calculated using the Hartree-Fock ionic core potentials tabulated by Garvey *et al.* [31], which tends to $-Q_p/|\vec{r}-\vec{R}(t)|$ at large separations. V_{pe}^I can be expressed in terms of the dynamic screening potential [Eq. (A8)] as

$$V_{pe}^I=-Q_pV^I(\vec{v}_{p_\parallel},R_z,\vec{s}) \tag{21}$$

As an additional perturbation, we include the effective velocity dependence of the surface barrier potential that determines the channel potentials near the surface [Eqs. (16) and (18)]. The static potential V_b [Eq. (16)] contains exchange and correlation effects of the interacting electron gas. Clearly, the electron exchange and correlation contribution to the barrier should decrease with increasing electron velocities above the Fermi velocity. The velocity dependence in the region outside the surface can be estimated from the velocity dependence of the electronic self-image potential $V_e^{\rm SI}$, which can also be expressed in terms of the dynamic screening potential as

$$V_e^{\rm SI}=\tfrac{1}{2}V^I(\vec{v}_{e_\parallel},z,z\hat{z}). \tag{22}$$

We correct for the effective velocity dependence the barrier potential by including the velocity dependent perturbation

$$\Delta V_b(v_e,z)=\begin{cases}0, & v_e<v_e^0\\ V_e^{\rm SI}(v_e,z)-V_e^{\rm SI}(v_e^0,z), & v_e>v_e^0,\end{cases} \tag{23}$$

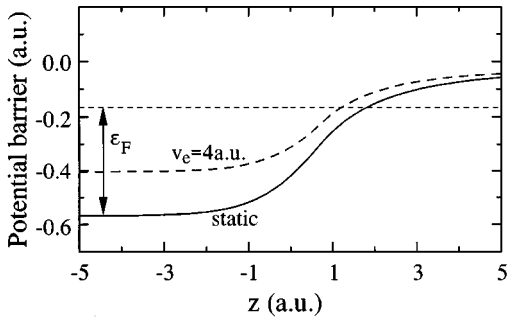

FIG. 4. Velocity dependence of the surface barrier potential for fast electrons due to the velocity dependence of the dynamical image part of the exchange and correlation potential.

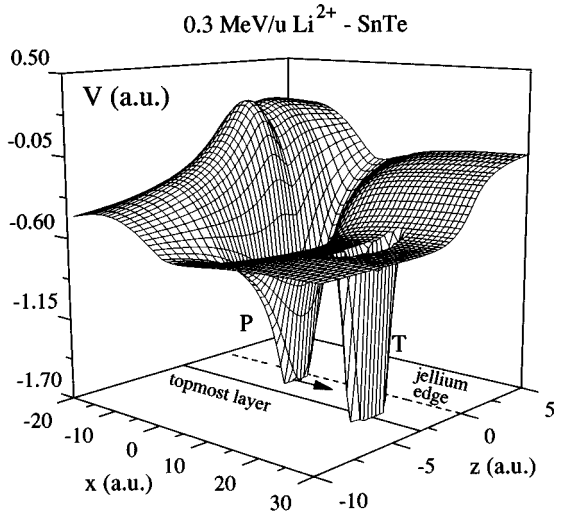

FIG. 5. Potential for an electron initially in a target core (T) near a 0.3-MeV/u Li^{2+} ion (P) moving parallel to a SnTe(001) surface as a function of the position vector of the electron $(x,y=1,z)$. The position of the projectile is $(0,0,-1)$ and the target core is at $(20,0,-z_J)$.

where a value $v_e^0=1.5$ a.u. has been chosen such that our model for the self-image interaction agrees with more accurate calculations using more sophisticated dielectric functions [33]. Since the self-image interaction is proportional to v_e^{-1}, the dynamic barrier is smaller than the static barrier (see Fig. 4). However, we have found that this dynamic correction has only a minor effect on our simulation results and, typically, only causes a change of the yield of convoy electrons of $\sim 20\%$.

In Fig. 5 we display the total potential experienced by an electron initially in a target core state near a Li^{2+} ion moving parallel to a SnTe(001) surface. In addition to the core fields of the target (T) and the projectile (P), the wake pattern and the surface barrier potential V_b [Eq. (16)] are also clearly visible.

D. Stochastic perturbation

The electronic Hamiltonian [Eq. (3)] contains a stochastic term that allows the incorporation of dissipative processes, i.e., energy loss, energy, and angular straggling. Within a Monte Carlo approach to the classical transport theory [22], dissipation can be included in terms of a stochastic force [Eq. (3)]:

$$\vec{F}_{\rm st}(t)=\sum_{\alpha}\sum_{j}\Delta\vec{p}_j^{\,\alpha}\delta(t-t_j^{\alpha}). \tag{24}$$

The determination of $F_{\rm st}(t)$ is thereby reduced to that of a stochastic sequence of pairs $(\Delta\vec{p}_j^{\,\alpha},t_j^{\alpha})$, i.e., momentum transfers $\Delta\vec{p}_j^{\,\alpha}$ delivered to the electron at times t_j^{α}. Any dependence of this sequence on the phase-space coordinates of the electron is treated as a parametric dependence, which does not affect the Langevin equations of motion. The explicit determination of the stochastic sequence $(\Delta p_j^{\alpha},t_j^{\alpha})$ depends on the choice of the differential inverse mean free paths (DIMFP), or equivalently, the probability density of energy transfers, $\omega=\Delta E=v_e^2/2-v_e'^2/2$ and momentum transfers, $\vec{q}=\Delta\vec{p}=\vec{v}_e'-\vec{v}_e$, to an electron during a single collision with velocities $\vec{v}_e$ and $\vec{v}_e'$ before and after the collision, respectively. Determination of DIMFP's near the surface is complicated by the fact that translation symmetry along the surface normal is broken. We discuss in the following briefly their construction in the case of grazing incidence. Further details are given in Appendix B.

Three mechanisms will be considered: elastic scattering ($\alpha=e$) and the bulk ($\alpha=i_b$) and surface ($\alpha=i_s$) contributions to inelastic scattering. The path between two adjacent collisions of the same type α is assumed to be a Poissonian distributed variable related to the mean free path, λ_α,

$$P_\alpha(\lambda)=\lambda_\alpha^{-1}e^{-\lambda/\lambda_\alpha}. \tag{25}$$

This assumption is strictly justified only for a homogeneous medium. Near the surface, λ_α is treated as a function of time through the temporal variations of v_e and z, which corrects, to some extent, for the inhomogeneity.

For target-elastic scattering at atomic cores, surface effects are not considered to be important since for small impact parameters the spherical atomic potential dominates. We evaluate the elastic DIMFP by an exact phase-shift analysis of elastic scattering of electrons at Sn and Te isolated atoms. However, in order to accomplish an efficient sampling for the probability distribution $P_{\rm el}(q)$ of momentum transfers we fit $P_{\rm el}(q)$ (or the DIMFP) to an analytic form derived from the Born approximation for a two-term Yukawa potential of the form $V_y(r)=-[Z_1\exp(-k_1r)+Z_2\exp(-k_2r)]/r$. Thus, our elastic DIMFP takes the form

$$\begin{aligned}\lambda_e^{-1}P_{\rm el}(q)&=\frac{d\lambda_e^{-1}}{dq}\\&=C(v_e)\frac{8\pi n_t q}{v_e^2}\left(\frac{Z_1}{q^2+k_1^2}+\frac{Z_2}{q^2+k_2^2}\right)^2\\&\quad\times\Theta(q_m-q),\end{aligned} \tag{26}$$

where $n_t=(2z_J)^{-3}$ is the volume number density of target nuclei and $C(v_e)$, $Z_{1,2}$, and $k_{1,2}$ are fitted to the exact DIMFP. We choose the parameters $Z_1=39.7$, $Z_2=11.3$, $k_1=4.0$, and $k_2=1.09$. The existence of the interface is taken into account by using an upper cutoff for the maximum momentum transfer $q_m(b)$ related to the distance $b=z+z_J$ to the topmost layer. We invoke the classical relationship between the impact parameter and the momentum transfer for effective Coulomb interactions, i.e., b represents the minimum impact parameter (giving rise to the maximum momentum transfer) for binary electron-target atom collisions.

Our description of the inelastic momentum and energy transfer distribution $P_i(\vec{q},\omega)$ near a surface is a natural extension of the well-known results for the bulk. For translation-invariant systems, the DIMFP (or probability density) in the Born approximation is related to the dielectric response function $\epsilon(q,\omega)$ via the dissipation-fluctuation theorem [34–36]

$$\lambda_i^{-1}P_i(\vec{q},\omega)=\frac{d^4\lambda_i^{-1}}{d^3q\,d\omega}$$
$$=\frac{1}{v_e\pi^2q^2}\mathrm{Im}\left(\frac{-1}{\epsilon(q,\omega)}\right)\delta\left(\omega-\vec{v}_e\cdot\vec{q}+\frac{q^2}{2}\right)$$
$$\times\Theta\left(\frac{v_e^2}{2}-\epsilon_F-\omega\right), \tag{27}$$

or, equivalently,

$$\frac{d^2\lambda_i^{-1}}{dq\,d\omega}=\frac{2}{v_e^2\pi q}\mathrm{Im}\left(\frac{-1}{\epsilon(q,\omega)}\right)\Theta[\omega_m(q)-\omega], \tag{28}$$

where $\omega_m(q)=\min[v_e^2/2-\epsilon_F;v_eq-q^2/2]$. An intuitive derivation of Eq. (27) makes use of the fact that the scattering probability per unit time (the fluctuation) is proportional to the energy loss per unit time, dW/dt, by the retarding force of the dynamic screening potential (the dissipation) yielding Eq. (27) up to the recoil term ($\sim q^2/2$) in the energy conserving δ function, $dW/dt=\vec{v}_{e_\parallel}\cdot\vec{\nabla}V^I_{\mathrm{bulk}}(\vec{p},z,z\hat{z})$ [see Eq. (A3)]. Note that unlike for the elastic DIMFP, Eq. (28) is a two-dimensional distribution function.

For grazing incidence collisions, Eq. (27) can be extended to near the surface by making use of the fact that translation symmetry is preserved in the plane along the beam direction for the jelliumlike valence-band electron density outside the ionic cores of surface atoms. We separate the inelastic DIMFP into two terms: a ''surface'' term ($\alpha=i_s$) and a ''bulk'' term ($\alpha=i_b$). Using a local surface dielectric function [37], $\epsilon(Q,\omega)$, the ''surface'' triply DIMFP associated with the surface term of the expression for the dynamic screening potential [Eq. (A5)] is given by

$$\frac{d^3\lambda_{i_s}^{-1}}{d^2Q\,d\omega}=\frac{e^{-2Q|z|}}{v_{e_\parallel}\pi Q}\mathrm{Im}\left(\frac{1-\epsilon(Q,\omega)}{\epsilon(Q,\omega)+1}\right)\delta\left(\omega-\vec{v}_{e_\parallel}\cdot\vec{Q}+\frac{Q^2}{2}\right)$$
$$\times\Theta\left(\frac{v_{e_\parallel}^2}{2}-\epsilon_F-\omega\right), \tag{29}$$

where we use the notation $\vec{q}=(\vec{Q},q_z)$.

The ''bulk'' DIMFP is constructed such that (i) it asymptotically tends to Eq. (27) when the electron is inside the solid, (ii) it tends to zero near the jellium edge, and (iii) it approximately incorporates the bulk term in the expression for the dynamic screening potential [Eq. (A3)]. A reasonable choice is

$$\frac{d^4\lambda_{i_b}^{-1}}{d^3q\,d\omega}=\frac{(1-e^{-2q|z|})}{v_e\pi^2q^2}\mathrm{Im}\left(\frac{-1}{\epsilon(q,\omega)}\right)\delta\left(\omega-\vec{v}_e\cdot\vec{q}+\frac{q^2}{2}\right)$$
$$\times\Theta\left(\frac{v_e^2}{2}-\epsilon_F-\omega\right), \tag{30}$$

where the factor $(1-e^{-2q|z|})$ yields both the exact DIMFP [Eq. (27)] in the bulk and a vanishing DIMFP at the surface ($z=0$). Details for the evaluation of Eqs. (29) and (30) are given in Appendix B.

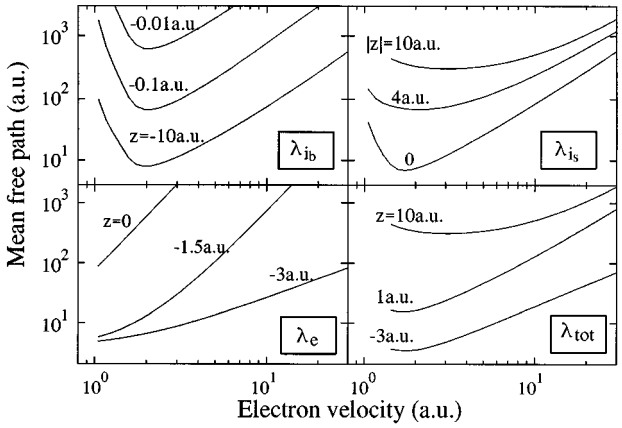

FIG. 6. Total, λ_{tot}, and partial mean free paths for elastic, λ_e, surface inelastic, λ_{i_s}, and bulk inelastic, λ_{i_b}, collisions as a function of the electron velocity for different positions of the electron, z, with respect to the jellium edge.

Figure 6 depicts the mean free paths λ_{is}, λ_{ib}, and λ_e used in our simulation as a function of the electron velocity for different fixed distances z from the surface. In each case we have assumed a trajectory parallel to the surface. In the velocity range of interest in this work ($2.8\leqslant v_e\leqslant 6$ a.u.), the total mean free path $\lambda_{\mathrm{tot}}=(\lambda_{i_s}^{-1}+\lambda_{i_b}^{-1}+\lambda_e^{-1})^{-1}$ can be as small as 5–10 a.u. Whenever the electron is above the topmost layer ($z>-3$ a.u.), the dominant collision processes (i.e., the one with the smallest mean free path) are surface inelastic collisions reaching a peak near at the jellium edge ($z=0$). On the other hand, near or below the topmost layer ($z<-3$ a.u.) elastic and bulk inelastic collisions rapidly acquire the dominant role. Figure 7 displays the smooth transition across the surface of the total inelastic mean free path $\lambda_i=(\lambda_{i_s}^{-1}+\lambda_{i_b}^{-1})^{-1}$ as a function of z for different velocities. In the limit $z\to-\infty$ the bulk limit is recovered while for $z\to\infty$ the mean free path tends to infinity because of the rapidly decreasing probability for excitation of particle-hole pairs or surface plasmons at large distances from the surface. At large but finite distances, the inelastic mean free path is

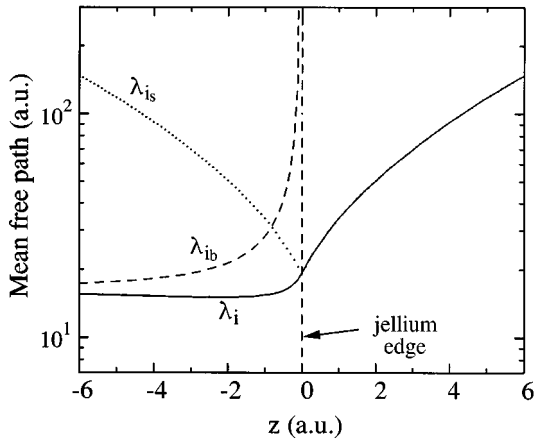

FIG. 7. Total inelastic mean free path $\lambda_i=(\lambda_{i_s}^{-1}+\lambda_{i_b}^{-1})^{-1}$ and its bulk ($\lambda_{i_b}^{-1}$) and surface ($\lambda_{i_s}^{-1}$) contributions as a function of z for an electron velcity $v_e=4$ a.u. parallel to the surface.

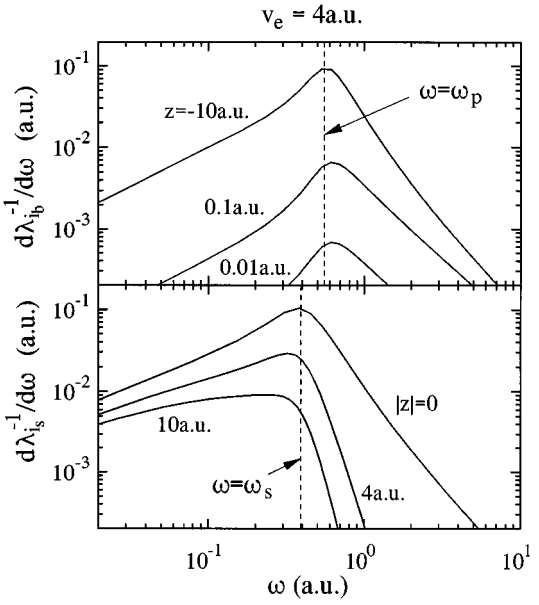

FIG. 8. Single DIMFP's as a function of the energy transfer for an electron velocity $v_e=4$ a.u. and for different distances of the electron, z, from the jellium edge.

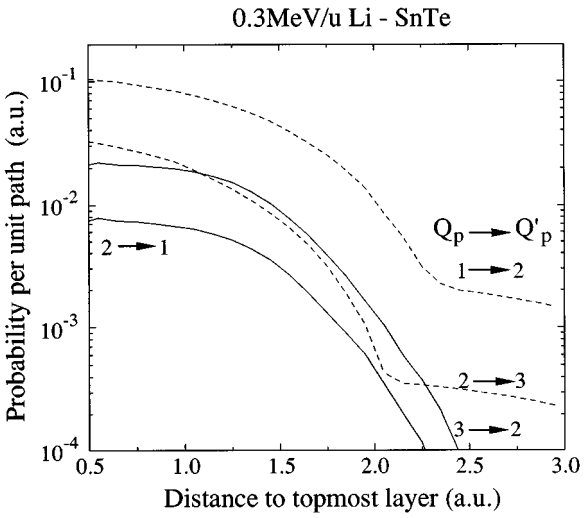

FIG. 9. Probability per unit path length along the surface for the charge changing reactions $Q_p \rightarrow Q_p'$ during the interaction of 0.3-MeV/u Li ions with SnTe surfaces as a function of the distance from the topmost atomic layer.

determined by optical (dipole) excitations of surface plasmons in the jellium surface. Analysis of the DIMFP as a function of the energy transfer (Fig. 8) shows that the most probable energy transfers associated with λ_{i_b} and λ_{i_s} are bulk and surface plasmon excitations with $\omega \simeq \omega_p$ and $\omega \simeq \omega_s = \omega_p/\sqrt{2}$, respectively.

IV. CHARGE-STATE EVOLUTION

The time dependence of the charge state, $Q_p(t)$, of the projectile ion during the glancing angle scattering is a key input quantity for the electronic evolution since it determines both the strength of the asymptotic Coulomb interaction between target electrons and the projectile in V_p^c as well as the indirect interaction through the image potential term V_{pe}^I [Eq. (21)]. Specifically, the value of Q_p influences the amount of shift of the convoy electron peak and the absolute yield of electrons. We have therefore performed a simulation of the charge-state evolution using the same theoretical input as for the dynamics of the electron emission, as discussed above, focusing, however, on the transient occupation of low-lying bound states rather than continuum states of the projectile.

As the impinging ion approaches the surface, its ionic charge state fluctuates in time due to (i) capture of electrons from the solid into bound states of the ion and (ii) ionization of electrons in bound states of the projectile caused by collisions with particles in the solid. In general, the local value of $Q_p(t)$ is a function of its initial charge state $[Q_p(t=t_0)]$ and the capture and loss probabilities near the surface. The corresponding transition probabilities per unit path length, $dP^{Q_p,Q_p'}/dR_x$ for charge changing $Q_p \rightarrow Q_p'$ are obtained from the description for binary atomic collisions: (i) the present CTMC results for ionization of $Li^{1+}(1s^2)$ and $Li^{2+}(1s)$ ions in collisions with the screened target nuclei of SnTe, (ii) experimental data for ionization of Li ions by free electrons (see [38] and references therein), and (iii) present CTMC results for electron capture processes from the N shell of SnTe into the ground states of Li ions. If we denote the impact-parameter-dependent transition probability by $P_{\text{at}}^{Q_p,Q_p'}$ and assume a random location of target atoms in the

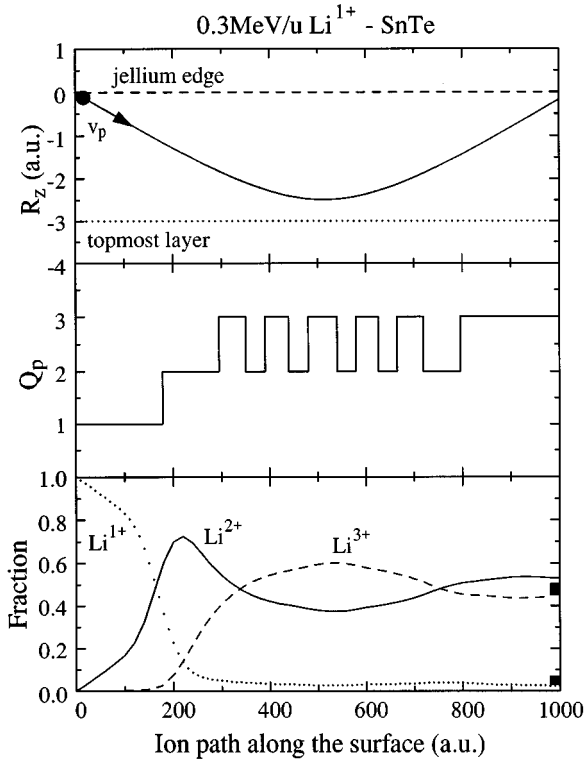

FIG. 10. The ionic trajectory, $R_z(R_x)$, the typical stochastic charge-state evolution, $Q_p(R_x)$, and the charge-state fractions for an incident 0.3-MeV/u Li^+ projectile on SnTe surfaces. The solid squares are experimental data of Kimura *et al.* [24] for outgoing charge-state fractions.

surface, the transition probability per unit path length for a trajectory (nearly) parallel to the surface at a distance d from the topmost layer is given by

$$\frac{dP_{\rm at}^{Q_p,Q_p'}}{dR_x}(d)=n_s^{\rm at}\int_{-\infty}^{\infty}dy\,P_{\rm at}^{Q_p,Q_p'}(\sqrt{y^2+d^2}). \tag{31}$$

For projectile ionization by target valence electrons treated as quasifree electrons, Eq. (31) should be replaced by

$$\frac{dP_{\rm el}^{Q_p,Q_p'}}{dR_x}(d)=n_v(d)\langle\sigma^{Q_p,Q_p'}\rangle, \tag{32}$$

where $\langle\sigma^{Q_p,Q_p'}\rangle$ is an average of the electron impact ionization cross section over electrons in the valence band and $n_v(d)$ is the classical density of target valence electrons near the surface. The total transition probabilities $dP^{Q_p,Q_p'}/dR_x$ per path length for the interaction of 0.3-MeV Li ions with a SnTe surface implies a very rapid fluctuation of the charge state (Fig. 9). The present transition rates are in reasonable agreement with the calculations of Kimura *et al.* [24] and Fuji *et al.* [39] based on the Bohr-Linhard model. Using Eqs. (31) and (32) as inverse mean free path lengths, a Poissonian stochastic process [Eq. (25)] for charge-state fluctuations can be calculated, an example of which is shown in Fig. 10. In a typical charge changing cycle, Q_p changes about 12 times. Therefore, memory of the initial charge state is completely lost, not only when the final charge state is reached but already during the interaction process in the vicinity of the surface.

Neglecting multiple electron processes, the evolution of the charge-state fractions $F_{Q_p}(R_x)$ is given by a system of coupled rate equations

$$\frac{d}{dR_x}F_{Q_p}(R_x)=\sum_{Q_p'=Q_p\pm1}\left(\frac{dP_{el}^{Q_p'Q_p}(R_x)}{dR_x}F_{Q_p'}(R_x)-\frac{dP_{el}^{Q_pQ_p'}(R_x)}{dR_x}F_{Q_p}(R_x)\right). \tag{33}$$

The resulting charge-state fractions for a 0.3-MeV/u Li^+ ion impinging on SnTe (Fig. 10) displays an abrupt decrease of the charge-state fraction of Li^+ ions from a value of one to almost zero before the projectile reaches a distance of 1.5 a.u. from the topmost layer. Subsequently, a quasi-charge-state equilibration is achieved yielding charge-state fractions of Li^{2+} and Li^{3+} of about 50%, which persists until exit. The final charge-state fractions are in agreement with experimental data [24]. Moreover, indirect evidence exists that charge-state equilibration is rapidly reached while the projectile is still in close proximity to the surface. By measuring the spectra of ejected electrons in coincidence with the final charge state of the emerging projectiles, Kimura *et al.* [24] recently found evidence consistent with a very rapid charge-state fluctuation and equilibration near the surface. Specifically, no correlation was found between the position of the convoy peak and the outgoing charge state of the ion.

The rapid charge-state fluctuations and the large number of charge-changing cycles along the trajectory considerably simplify the simulation of the electron evolution: Initially loosely bound projectile electrons at $t=t_0$ can be neglected since a larger number of transient projectile electrons are produced as a result of electron capture. Furthermore, rather than following simultaneously the evolution of the charge state and of ionized electrons we can calculate the spectra of fast electrons as a weighted average of the spectra obtained for the different fixed ionic charge states, where the weights are given by the equilibrium charge-state fractions, which should closely resemble the local values during emission.

V. ELECTRON EMISSION

The doubly differential emission spectrum as a function of the Cartesian components of the velocity vector is displayed in Figs. 11 and 12 for 0.3-MeV/u Li ions scattering of a SnTe surface. Figure 11 displays a cut in the velocity plane (v_x,v_y) parallel to the surface while Fig. 12 corresponds to a (v_x,v_z) cut in the scattering plane. The void in the center of Figs. 11 and 12 is due to the fact that we consider only fast electrons with $v_e>v_p/\sqrt{2}$. In order to clearly identify different structures, the total ejected electron spectrum has been decomposed into the components originating from valence band and from core levels. Both cuts clearly exhibit the ''binary ridge'' [40], well known from ion-atom collisions. This structure arises from quasi-two-body collisions between a target electron and the impinging ion. Because of the large mass of the ion, conservation of energy and momentum implies that the final velocity of an electron initially at rest will be $v_e=|\vec{v}_p+\vec{v}_p'|$, where $\vec{v}_p'$ has arbitrary direction and magnitude $v_p'=v_p$. This corresponds to a sphere centered at $v_e=v_p$ with a radius equal to v_p. The location of such a ''binary sphere'' agrees with the region of highest density

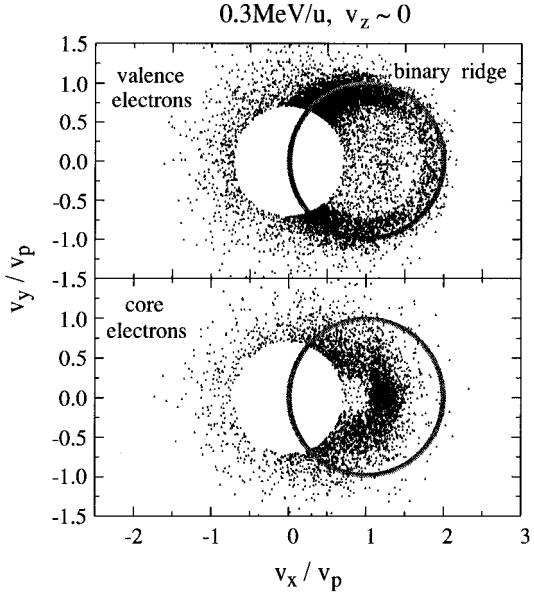

FIG. 11. Density plot in velocity space of ejected valence or core electrons arising from 0.3-MeV/u Li-SnTe collisions cut in the (v_x,v_y) plane parallel to surface. The thick line indicates the location of the binary ridge.

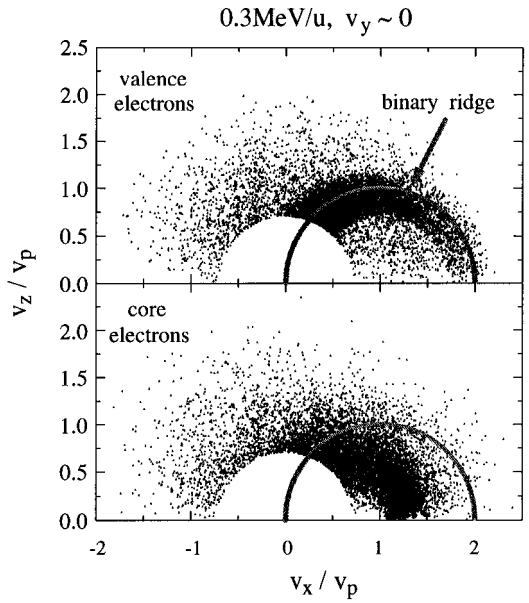

FIG. 12. As in Fig. 11, however, cut in the (v_x, v_z) scattering plane.

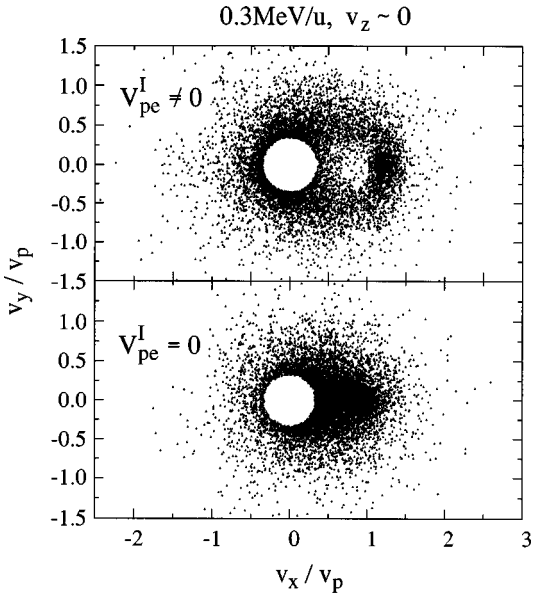

FIG. 13. Effect of the wake potential V^I_{pe} on the spectrum of ejected electrons. As in Fig. 11, however, sum of the core and valence electrons. Upper frame with V^I_{pe} and lower frame without V^I_{pe}.

for valence electrons but not for core electrons. The width of the sphere is due to the initial momentum distribution of electrons in the valence band. The absence of a comparable structure for core electrons is a direct consequence of their broad momentum distribution, which is comparable to the projectile velocity.

The spectrum of core electrons is seen to peak in the forward direction ($v_x >> v_y, v_z$) and for velocities $v_e \gtrsim v_p$. This region of high density corresponds to the so-called CEP for ion-surface scattering, which is caused by the attraction of the projectile field. The shift of the convoy peak to the $v_e > v_p$ region is generally believed to be a direct consequence of the image potential induced by the impinging ion V^I_{pe}. The microscopic mechanism leading to the peak can be viewed as rainbow scattering of electrons at the screened field of the ion V^I_{pe} [23]. In order to illustrate the dramatic effects introduced by this potential we give in Fig. 13 a comparison of our full simulation with a simulation with V^I_{pe} turned off. Inclusion of the image of the ion not only broadens and shifts the highest density region from $v_x \simeq v_p$, $v_y \simeq 0$ to $v_e > v_p$ but causes a pronounced void in the forward electron spectrum near the region $v_e \simeq v_p$. This depletion is a direct consequence of the expulsion of ejected electrons by the repulsive first half-wave of the induced wake potential in the immediate vicinity of the ion. It should be emphasized that this void is not due to losses by multiple scattering near the surface, which is included in both calculations of Fig. 13.

We expect that similar effects should also take place even if the ion undergoes subsurface channeling one or two layers inside the solid. If the escape path of the electron is of the order of or smaller than a mean free path, structures associated with the scattering of electrons at the wake should also be visible, though broadened. This is possibly the reason why the shift of the convoy electron peak could even be observed for surfaces that were not very well characterized and flat.

We note that an alternative explanation of the shift of the convoy peak has recently been proposed by Baragiola [14] who suggested that this could be a local charge effect due to the large number of electrons emitted per impinging ion. The underlying picture is that, typically, of the order of a hundred slow electrons are emitted per ion giving rise to a large negatively charged cloud trailing the ion and whose repulsive potential would accelerate convoy electrons to larger energies. We have estimated the size of this effect and found it to be negligible compared to the wake potential. This is due to the fact that for every slow electron emitted, there will be, dependent on the conductivity of the surface, a hole or an induced image charge with a charge of $+1$. Therefore, the long-range behavior of the resulting perturbation is dipolelike rather than Coulomb-like. Because the center of the charge cloud lags behind a large distance from the ion, the effect of such a dipolelike potential is small.

The doubly differential absolute yield of ejected electrons as a function of the emission energy at various emission angles $\theta = \cos^{-1}(v_x/v_e)$ (Fig. 14) is broken down into three distinct components: emission of valence electrons, direct emission of core electrons, and emission of electrons transiently bound to the projectile but originating from target cores. The most striking observation is that valence electrons represent only a very small fraction of the total yield of fast electrons for the present collision system. Consequently, the sharp binary ridge structure for emission of valence electrons (Figs. 11 and 12) shows up only as a shoulder in the total yield of electrons. The most discernible structure of the total spectrum is the convoy electron peak at small emission angles, which is primarily due to direct excitation of target core states. The dominance of core electron emission in the spectrum of fast electrons is in part due to the larger multiplicity by a factor ~ 3.6 of active core electrons in the N-shell of Sn or Te compared to valence electrons. More importantly, the ion velocities considered in this work, $v_p \sim 3-4$ a.u., are close to the matching velocities of target core electrons in the N shell of SnTe (see Table I). Since

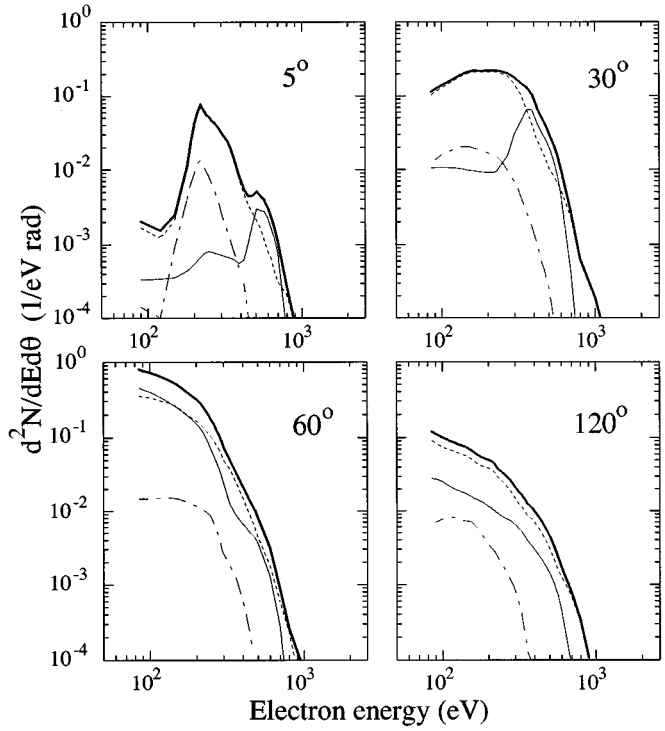

FIG. 14. Doubly differential yield of electrons per impinging ion in 0.3-MeV/u Li-SnTe collisions as a function of the electron energy for different emission angles with respect to the x axis: total yield (thick solid line), valence electrons (thin solid line), core electrons (dashed line), electrons that were transiently captured to bound states of the ions (dashed dotted line).

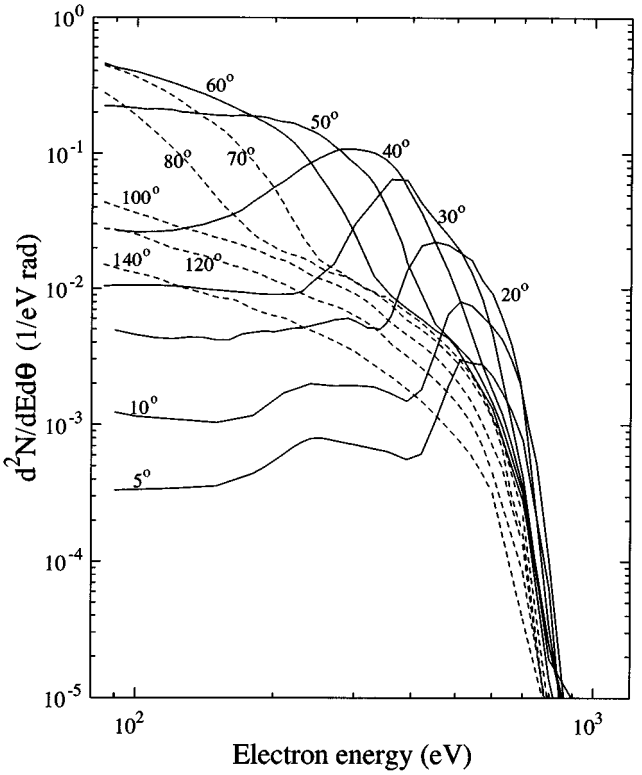

FIG. 15. Doubly differential yield of valence electrons per impinging ion in 0.3-MeV/u Li-SnTe collisions as a function of the electron energy for different emission angles.

direct electron capture from target states into low-lying continuum states of the projectile relies on the overlap of the momentum distributions of projectile and target states [41], core electrons in the N shell are strongly favored in complete analogy to electron capture in atom collisions (see, e.g., [42]). By contrast, direct ionization of valence electrons into states with velocities $\vec{v}_e \sim \vec{v}_p$ is very unlikely since the initial velocities of electrons in the valence band, which are smaller than the Fermi velocity ($v_F \sim 0.9$ a.u.), are small compared to v_p. In other collision systems, emission of valence or conduction electrons may dominate, e.g., collisions at lower velocities [13] or experiments involving lighter target atoms such as pyrolytic graphite surfaces [43]. The latter target has only two core electrons per atom, which are very tightly bound and possess orbital velocities of ~ 6 a.u. Therefore, experiments involving ions with a few hundred keV/u energies will predominantly ionize valence electrons resulting in a pronounced binary peak.

While direct excitation of a valence electron into convoy states is quite unlikely, valence electrons may eventually end up in the region of the convoy peak as a consequence of electron transport, i.e., multiple scattering. Loosely speaking, this process is analogous to Thomas scattering in ion-atom collisions, in which electron capture of a quasi-free-electron takes place by a double-scattering sequence, first at the projectile and subsequently at the target. In the present case, the two scattering events are separated in time and space and take place on the energy shell. The second scattering center is provided by the array of target nuclei in the surface. The broad convoy peak originating from valence electrons (Figs. 14 and 15) results from this multiple-scattering sequence.

Multiple scattering is also important in other regions of the ejected electron spectrum, for example, for emission of energetic valence electrons at large angles (Fig. 15). They originate from binary encounter electrons, which are first emitted towards the inside of the solid and are subsequently scattered at target cores. At an emission angle of 60°, this pathway to electron emission gives rise to a shoulder in the energy distribution of ejected valence electrons at an energy that is larger than that of the direct binary peak at the same angle [i.e., $2v_p^2\cos^2(60°)$]. A similar effect has been observed in transmission experiments [44]. Furthermore, multiple scattering is responsible for ionizing core electrons, which are transiently captured to bound states of the projectile contributing 10–20% of the convoy yield.

In Fig. 16 we compare the results of our simulation, summed over all contributions from the core and valence electrons, with measurements for the triply differential yield of ejected electrons. Our simulation predicts a pronounced convoy electron peak that is considerably shifted to energies larger than the nominal convoy peak energy $E/E_i = 1$. The peak position and width are in reasonable agreement with experiment but the calculated shifts are slightly larger than the experimental ones. At present, the origin of this discrepancy is not well understood.

The calculations in Fig. 16 consist of a weighted average of the spectra obtained for Li^+, Li^{2+}, and Li^{3+} ions (Fig. 17). These fractions for $Q_p = 1,2,3$ are 10%, 65%, and 25% at 0.2 MeV/u, 4%, 48%, and 48% at 0.3 MeV/u, and 0%, 25%, and 75% at 0.5 MeV/u, respectively. Because the yield

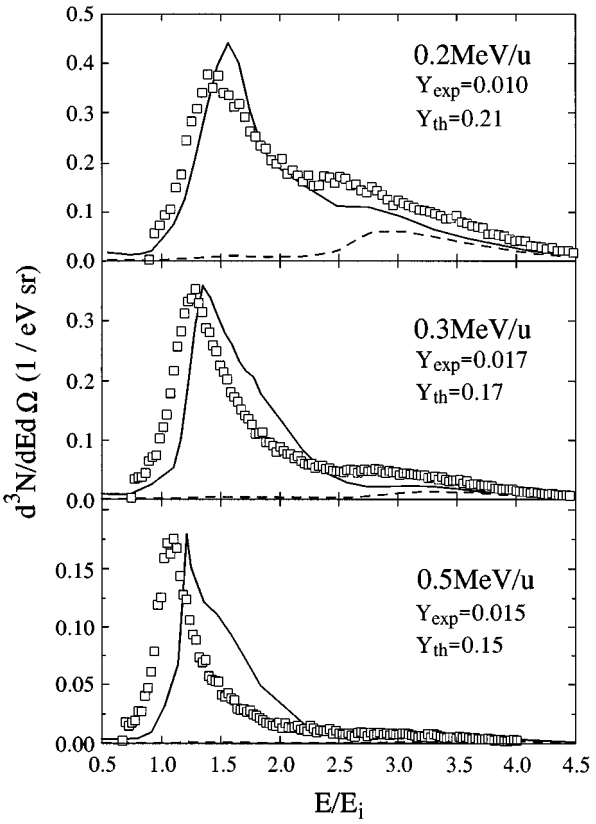

FIG. 16. Triply differential yield of electrons emitted at $\theta=98$ mrad in the (x,z) plane in a solid angle of 100×100 mrad^2 resulting from the interaction of 0.2-, 0.3-, 0.5-MeV/u Li ions with SnTe(001): calculated total yield (solid lines), calculated yield of valence electrons (dashed lines), and experiment (open circles). The experimental data [24] have been normalized to theory. The calculated and experimentally estimated yields per ion within the full width at half maximum are given by $Y_{\rm th}$ and $Y_{\rm expt}$, respectively.

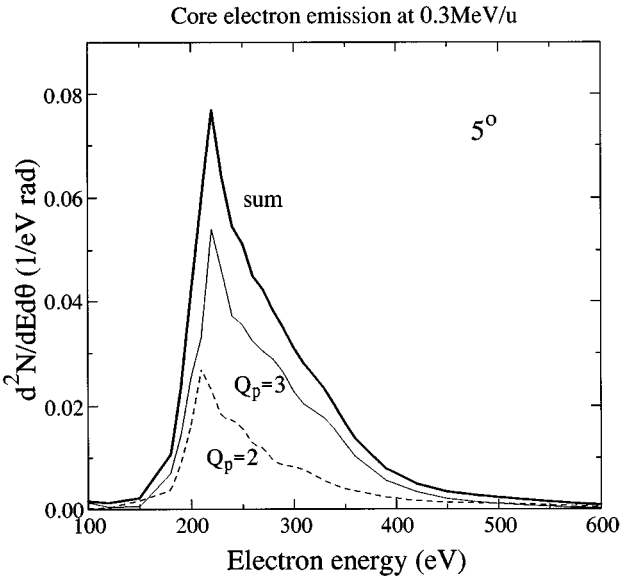

FIG. 17. Projectile charge dependence of the convoy electron peak in 0.3-MeV/u Li-SnTe collisions.

of convoy electrons is proportional to $Q_p^{\gamma}(\gamma\simeq2)$, the relative contribution of the highest charge state is favored. The convoy peak for $Q_p=2$ (Fig. 17) is less shifted than that for $Q_p=3$, which is a consequence of the fact the image potential is proportional to Q_p. The present simulation features a relatively weak Q_p dependence. The first proposed model of convoy electron acceleration predicted a shift proportional to (Q_p-1) [9]. The present simulation does not follow this dependence and it even predicts a shift for $Q_p=1$ that disagrees with experimental findings for protons. Thus, the simulation appears to somewhat overestimate the shift of the CEP (see also Fig. 16).

Absolute yields of ejected electrons would provide a very sensitive and critical test of theoretical models. Unfortunately, no published data for absolute convoy electron yields are available in the literature because several aspects affecting the normalization of the experimental yields are not well understood (e.g., efficiency of the electron spectrometer, effective target region that interacts with the incident beam, etc.). We have therefore normalized the data in Fig. 16 to the calculations. Nevertheless, we can compare our absolute yields $Y_{\rm th}$ with preliminary estimates of experimental yields kindly provided to us [45] and displayed as $Y_{\rm exp}$ in Fig. 16. The striking result of the comparison between theory and experiment is that the calculated yields are about an order of magnitude larger than the measurements. We estimate our yields to be accurate to within a factor of ~3. At this moment, no convincing explanation can be put forward to reconcile this discrepancy. Experiments currently underway at ORNL using Si targets [16] may shed some light on the absolute convoy yields in the near future.

VI. CONCLUDING REMARKS

In this work we have introduced a classical trajectory Monte Carlo approach to describe the emission of fast kinetic electrons ($v_e>2v_F$) in fast glancing-angle ion-surface collisions. The present theory differs from previous approaches in that (i) we include both core and valence electrons in our microscopic treatment on equal footing and (ii) we explicitly treat the transport and multiple scattering of electrons near the surface. This allows us to calculate absolute yields of electrons and to evaluate the relative contribution of the different sources of electrons as well as to analyze the relative importance of the different microscopic processes electrons undergo prior to emission. Our results for the shape of the convoy electron peak at forward emission angles are found to be in reasonable agreement with recent experiments. However, there is a sizable discrepancy in the absolute yields of convoy electrons from ion-surface collisions that remains to be understood.

We have shown that the spectrum of ejected electrons exhibits clear signatures of image interactions near the surface. Employing the hydrodynamical model [46] for the induced potential to treat nonlinear effects in the regime of strong perturbation $Q_p/v_p\simeq1$ appears an attractive pathway for improvement of the simulation. A realistic quantum mechanical treatment for convoy electron emission for the present collision systems remains a major challenge.

ACKNOWLEDGMENTS

Support for this work has been provided by the U.S. Department of Energy, Office of Basic Energy Sciences, Division of Chemical Sciences, under Contract No. DE-AC05-96OR22464 with ORNL managed by Lockheed Martin Energy Research Corp. and by the NSF. We gratefully acknowledge useful discussions with K. Kimura, M. Mannami, R. Pfandzelter, H. Winter, S. Elston, R. Minnitti, H. Lebius, J. Kim, J. Garcia de Abajo, and R. Baragiola.

APPENDIX A: DYNAMIC SCREENING POTENTIALS

A quantity of key importance of the present simulation is the dyanmic screening potential $V^I(\vec{v},R_z,\vec{s})$ from which the self-image potential of the projectile ion [Eq. (14)], the self-image potential of the electron [Eq. (22)], and the indirect interaction between the projectile and the electron, V^I_{pe}, via charge density fluctuations in the surface [Eq. (21)] can be derived. Since a very large number of evaluations of the potential and the corresponding forces are required in the simulation ($>10^{10}$), a compromise between accuracy and computational simplicity must be struck. We give here a few technical details of the evaluation of V^I.

We employ linear response theory using the so-called specular reflection model [33]. Within this approximation, the induced potential is given by the solution of the Poisson equation for a moving particle near a ''surface'' (the jellium edge), which separates vacuum and a material described by a dielectric response function $\epsilon(k,\omega)$. Assuming that the parallel and perpendicular velocity components of the particle satisfy the relation $v_\parallel \gg v_\perp$, the corresponding induced potential per unit charge at a position $\vec{s}$ is given by [33]

$$V^I(\vec{v},z_0,\vec{s})=V^I_{\rm surf}(\vec{v},z_0,\vec{s})+\Theta(-z)\Theta(-z_0)V^I_{\rm bulk}(\vec{v},z_0,\vec{s}), \tag{A1}$$

with

$$V^I_{\rm surf}(\vec{v},z_0,\vec{s})=\frac{1}{2\pi}\int\frac{d^2K}{K}e^{i\vec{K}\cdot\vec{S}}\left\{\Theta(z_0)\left[\Theta(z)\left(\frac{\epsilon_s(K,\omega)-1}{\epsilon_s(K,\omega)+1}e^{-K(z+z_0)}\right)+\Theta(-z)\left(\frac{2\epsilon_s(K,z,\omega)}{\epsilon_s(K,\omega)+1}e^{-Kz_0}\right)\right]\right.$$
$$\left.+\Theta(-z_0)\left[\Theta(z)\left(\frac{2\epsilon_s(K,z_0,\omega)}{\epsilon_s(K,\omega)+1}e^{-Kz}\right)+\Theta(-z)\left(\epsilon_s(K,z+z_0,\omega)-\frac{2\epsilon_s(K,z_0,\omega)}{\epsilon_s(K,\omega)+1}\epsilon_s(K,z,\omega)\right)\right]\right\}, \tag{A2}$$

$$V^I_{\rm bulk}(\vec{v},z_0,\vec{s})=\frac{1}{2\pi^2}\int\frac{d^3k}{k^2}e^{i\vec{k}\cdot[\vec{S}+(z-z_0)\hat{z}]}\left(\frac{1}{\epsilon(k,\omega)}-1\right)=\frac{1}{2\pi}\int\frac{d^2K}{K}e^{i\vec{K}\cdot\vec{S}}[\epsilon_s(K,z-z_0,\omega)-e^{-K|z-z_0|}], \tag{A3}$$

and

$$\epsilon_s(K,z,\omega)=\frac{K}{\pi}\int\frac{dk_z}{K^2+k_z^2}\frac{e^{ik_zz}}{\epsilon(k,\omega)}, \tag{A4}$$

where $\omega=\vec{v}\cdot\vec{K}\simeq vK_x$, $\Theta(z)$ is a step function, and we use the notation $\vec{k}=(\vec{K},k_z)$, $\vec{s}=(\vec{S},z)$. We have adopted a coordinate system moving with velocity $v_\parallel$ (Fig. 1) with the z coordinate of the particle given by z_0. The $V^I_{\rm bulk}$ component of the induced potential is the well-known induced potential in the bulk of a solid [36].

If plasmon dispersion along the z axis is neglected [i.e., $\epsilon(k,\omega)\simeq\epsilon(K,\omega)$, which implies $\epsilon_s(K,z,\omega)\simeq\epsilon^{-1}(K,\omega)e^{-K|z|}$], the induced potential reduces to

$$V^I_{\rm surf}(\vec{v},z_0,\vec{s})\simeq\frac{1}{2\pi}\int\frac{d^2K}{K}e^{i\vec{K}\cdot\vec{S}}\left\{\left(\frac{\epsilon(K,\omega)-1}{\epsilon(K,\omega)+1}e^{-K(|z|+|z_0|)}\right)-\Theta(-z_0)\Theta(-z)\left(\frac{1}{\epsilon(K,\omega)}-1\right)e^{-K(|z|+|z_0|)}\right\}, \tag{A5}$$

$$V^I_{\rm bulk}(\vec{v},z_0,\vec{s})\simeq\frac{1}{2\pi}\int\frac{d^2K}{K}e^{i\vec{K}\cdot\vec{S}}\left(\frac{1}{\epsilon(K,\omega)}-1\right)e^{-K|z-z_0|}. \tag{A6}$$

The complete anisotropy of the induced potential near the surface greatly complicates its implementation in a Monte Carlo simulation. A four-dimensional tabulation of the potential would be required to treat a collision for a given impact energy. For this reason, equations (A1)–(A6) with k dependent response functions are used only to treat dissipative processes (see Sec. III D and Appendix B). Our induced potentials are instead calculated using a frequency-dependent dielectric function without dispersion (e.g., [33,36]),

$$\epsilon(\omega)=1-\frac{\omega_{pv}^2}{\omega(\omega+i\gamma)}, \tag{A7}$$

where $\omega_{pv}=\sqrt{4\pi n_v}$ is the classical plasma frequency of a free-electron gas with volume number density n_v and γ is an effective damping constant. For SnTe surfaces the free-electron gas corresponds to the valence band with $\omega_{pv}=0.555$ a.u. and $\gamma=0.314$ a.u. obtained from photoemission spectra [26]. Using Eq. (A7),

$$V^I(\vec{v},z_0,\vec{s})=\frac{\omega_{sv}}{v}V^+(\delta_s,x_s,\rho_s)+\Theta(-z)\Theta(-z_0)\frac{\omega_{pv}}{v}\times[V^+(\delta_p,x_p,\rho_p')-V^+(\delta_p,x_p,\rho_p)], \quad \text{(A8)}$$

with $\omega_{sv}=\omega_{pv}/\sqrt{2}$,

$$\delta_{s,p}=\frac{\gamma}{\omega_{sv,pv}}, \quad \text{(A9)}$$

$$x_{s,p}=\frac{\omega_{sv,pv}}{v}x, \quad \text{(A10)}$$

$$\rho_{s,p}=\frac{\omega_{sv,pv}}{v}\sqrt{y^2+(|z|+|z_0|)^2}, \quad \text{(A11)}$$

$$\rho'_{s,p}=\frac{\omega_{sv,pv}}{v}\sqrt{y^2+(z-z_0)^2}, \quad \text{(A12)}$$

$$V^+(\delta,x,\rho)=\Theta(x)F_{0,0}(\delta,|x|,\rho)+\Theta(-x)\left[F_{0,0}(-\delta,|x|,\rho)-\frac{4}{\sqrt{4-\delta^2}}e^{-\delta|x|/2}\sin(x\sqrt{4-\delta^2}/2)H_0(\delta,\rho)-2\delta e^{-\delta|x|/2}\cos(x\sqrt{4-\delta^2}/2)G_0(\delta,\rho)\right], \quad \text{(A13)}$$

$$F_{n,k}(\delta,x,\rho)=\int_0^\infty dq\,\frac{q^k J_n(q\rho)e^{-qx}}{1+q^2+q\delta}, \quad \text{(A14)}$$

$$G_n(\delta,\rho)=\int_0^\infty dq\,\frac{q^{n+1}J_n(q\rho)}{(1+q^2)^2-q^2\delta^2}, \quad \text{(A15)}$$

$$H_n(\delta,\rho)=K_n(\rho)+\frac{\delta^2}{2}\int_0^\infty dq\,\frac{q^{n+1}J_n(q\rho)(1+3q^2)}{[(1+q^2)^2-q^2\delta^2](1+q^2)}, \quad \text{(A16)}$$

where J_n and K_n denote Bessel and modified Bessel functions, respectively. The gradient of the potential can be easily expressed in terms of the functions $F_{0,1},F_{1,1},G_0,G_1,H_0$, and H_1. Note that the arguments of these functions depend only on reduced quantities, which greatly facilitates their tabulation.

Apart from its simplicity, our choice of the local dielectric function (A7) can be justified by the observation by Garcia de Abajo and Echenique [33] that for fast particles ($v>1.5v_F$) resulting self-image interactions are in extremely good agreement with the ones obtained using more elaborate models. Deviations are expected to occur, however, in V^I_{pe} for $x_s<0,\rho_s<1$. In this region the wake resulting from Eq. (A7) contains a logarithmic singularity in the limit $\rho_s\to 0$ due to the modified Bessel function in Eq. (A16), which is not present in calculations including dispersion [33,36]. This singular behavior is frequently circumvented by using a cutoff at $q=v_p/v_F$ in the integrals of Eqs. (A14), (A15), and (A16), however, at the price of an unphysical behavior of the induced potentials at large distances from the surface. Instead, we set the derivatives of H_0 and G_0 to a constant for $\rho<\rho_{\min}$ with $\rho_{\min}\simeq v_F/(3v_p)$. We have verified that our simulation is not sensitive to variations of $\rho_{\min}$ to within a factor of 3 around this value. We also note that an additional logarithmic divergence exists in the gradient of the potential through the function $F_{0,1}$ in the limits $x_s\to 0$ and $\rho_s\to 0$. However, in this region, the dynamics is governed by the stronger singularity of the Coulomb field of the projectile and this term is negligible.

At large separations $V_e^{\rm SI}$ and V^I_{pe} converge to classical Coulomb-like image interactions

$$V^I_{pe}\xrightarrow[x_s,\rho_s\to+\infty]{}-\frac{Q_p}{\sqrt{(z+|R_z|)^2+y^2+(x+\gamma v_p/\omega_{sv}^2)^2}}, \quad \text{(A17)}$$

$$V_e^{\rm SI}\xrightarrow[|z|\to+\infty]{}-\frac{\Theta(z)}{4z}-\frac{\Theta(-z)\omega_{pv}}{2v_{e_\parallel}\sqrt{4-\delta_p^2}}\times\left[\pi-2\tan^{-1}\left(\frac{\delta_p}{\sqrt{4-\delta_p^2}}\right)\right]. \quad \text{(A18)}$$

Figure 18 depicts the position of the corresponding image centers. The dynamic image of the projectile is characterized by the fact that the image charge lags behind the ion by a distance that is proportional to the ion velocity. Note, however, that the picture of Coulomb-like image interactions is only valid at large separations from the surface. Because of the choice (A7) for the dielectric function, the image plane coincides with the jellium edge. We have verified that our ejected electron spectra are insensitive to changes of ± 0.5 a.u. in the position of the jellium edge.

Equation (A8) should account for the polarization and dielectric response of core electrons since small distances d of the projectile from the top row of surface atoms significantly contribute. We employ a simple estimate of the polarization of core electrons in the dynamic screening potential in terms of an inhomogeneous electron gas with a local plasma frequency [47]

$$\omega_p^2(d)=\omega_{pv}^2+\sum_{n,l}4\pi\rho_{n,l}(d), \quad \text{(A19)}$$

where $\rho_{n,l}(d)$ denotes the planar-averaged number density of electrons in the state with quantum numbers n,l. The polarization of core electrons is accounted for using $\omega_p(d)$ instead of ω_{pv} in V^I_{pe}. Pitarke *et al.* [47] have successfully implemented this approach to explain the anomalously large shift

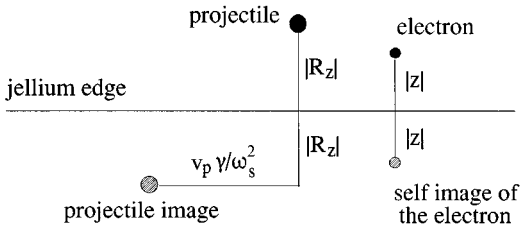

FIG. 18. Position of image charges at large distances.

of the radiative electron capture peak observed by Vane *et al.* [48] for titanium ions channeled in a gold single crystal. We have determined the electronic densities $\rho_{n\ell}$ entering Eq. (A19) from core states of isolated atoms with Hartree-Fock approximation [49].

APPENDIX B: COLLISION KERNELS

For the evaluation of the inelastic DIMFP's [Eqs. (29) and (30)], it is straightforward to incorporate dispersion effects into the dielectric response function. This is different from the calculation of V^I (see Appendix A). We therefore choose here the plasmon-pole approximation with dispersion and single-particle single-hole excitations for valence electrons:

$$\epsilon(q,\omega)=1+\frac{\omega_{pv}^2}{\beta^2 q^2+q^4/4-\omega(\omega+i\gamma)}, \tag{B1}$$

where $\beta=v_F\sqrt{3/5}$. We use the same dielectric function for $\lambda_{i_b}^{-1}$ and $\lambda_{i_s}^{-1}$ upon replacing q by Q. We point out that at small distances from the surface and speeds v_e comparable to the threshold for electron impact excitation of core electrons, contributions from inner shells to the DIMFP, neglected in the following, could possibly contribute as well.

Irrespective of the choice of $\epsilon(q,\omega)$, a two-dimensional probability distribution must be constructed. From Eqs. (29) and (30), the resulting doubly DIMFP as a function of the energy and momentum transfers are given by

$$\frac{d^2\lambda_{i_s}^{-1}}{dQ\,d\omega}=\frac{2e^{-2Q|z|}}{\pi\sqrt{Q^2v_e^2-\left(\omega+\frac{Q^2}{2}\right)^2}}\times\mathrm{Im}\left(\frac{1-\epsilon(Q,\omega)}{\epsilon(Q,\omega)+1}\right)\Theta[\omega_m(Q)-\omega], \tag{B2}$$

$$\frac{d^2\lambda_{i_b}^{-1}}{dq\,d\omega}=\frac{2}{v_e^2\pi q}(1-e^{-2q|z|})\mathrm{Im}\left(\frac{-1}{\epsilon(q,\omega)}\right)\times\Theta[\omega_m(q)-\omega]\Theta(-z). \tag{B3}$$

The random vectors $\vec{q}$ and $\vec{Q}$ can be obtained from random values of q,Q,ω and the energy transfer equations $\omega=\vec{q}\cdot\vec{v}_e-(q^2/2)$ or $\omega=\vec{Q}\cdot\vec{v}_e-(Q^2/2)$. In order to accomplish an efficient numerical sampling of energy and momentum transfers we make one additional approximation by neglecting the recoil term $Q^2/2$ term inside the square root in Eq. (B2). This permits the analytical integration of Eq. (B2) over ω.

[1] C. B. Crook and M. E. Rudd, Phys. Rev. Lett. **25**, 1599 (1970).
[2] K. G. Harrison and M. W. Lucas, Phys. Lett. **33A**, 142 (1970).
[3] Y. Yamazaki *et al.*, Phys. Rev. Lett. **61**, 2913 (1988).
[4] J. P. Gibbons *et al.*, Phys. Rev. Lett. **67**, 481 (1991).
[5] J. Burgdörfer and C. Bottcher, Phys. Rev. Lett. **61**, 2917 (1988); J. Kemmler, J. Burgdörfer, and C.O. Reinhold, Phys. Rev. A **44**, 2993 (1991).
[6] L. F. de Ferraris and R. Baragiola, Phys. Rev. A **33**, 4449 (1986).
[7] M. Hasegawa, K. Kimura, and M. Mannami, J Phys. Soc. Jpn. **57**, 1834 (1988).
[8] H. Winter, P. Strohmeier, and J. Burgdörfer, Phys. Rev. A **39**, 3895 (1989).
[9] J. Burgdörfer, Nucl. Instrum. Methods **24/25**, 139 (1987).
[10] A. Koyama *et al.*, Phys. Rev. Lett. **65**, 3156 (1990); A. Koyama, Nucl. Instrum. Methods **67**, 103 (1992); H. Ishikawa *et al.*, Nucl. Instrum. Methods **67**, 160 (1992).
[11] M. Hasegawa, T. Fukuchi, Y. Mizuno, K. Kimura, and M. Mannami, Nucl. Instrum. Methods B **53**, 285 (1991).
[12] K. Kimura, M. Tsuji, and M. Mannami, Phys. Rev. A **46**, 2618 (1992).
[13] E. A. Sánchez, O. Grizzi, M. L. Martiarena, and V. H. Ponce, Phys. Rev. Lett. **71**, 801 (1993).
[14] R. A. Baragiola, Nucl. Instrum. Methods B **78**, 223 (1993).
[15] T. Iitaka, Y. H. Ohtsuki, A. Koyama, and H. Ishikawa, Phys. Rev. Lett. **65**, 3160 (1990).
[16] H. Lebius, R. Minniti, J. Y. Lim, and S. Elston, Phys. Rev. A (to be published).
[17] F. Garcia de Abajo, V. H. Ponce, and P. Echenique, Phys. Rev. Lett. **69**, 2364 (1992).
[18] F. J. Garcia de Abajo, Nucl. Instrum. Methods **98**, 442 (1995); M. L. Martiarena, E. A. Sanchez, O. Grizzi, and V. H. Ponce, Phys. Rev. A **53**, 895 (1996); U. Thumm, J. Phys. B **25**, 425 (1992).
[19] D. R. Schultz, C. O. Reinhold, and R. E. Olson, in *Two Center Effects in Ion-Atom Collisions*, edited by T. J. Gay and A. F. Starace, AIP Conf. Proc. No. 362 (AIP, College Park, 1996), p. 84; C. O. Reinhold and R. E. Olson, Phys. Rev. A **39**, 3861 (1989); R. L. Becker and A. D. MacKellar, J. Phys. B **17**, 3923 (1984); C. O. Reinhold and C. A. Falcón, Phys. Rev. A **33**, 3859 (1986).
[20] C. O. Reinhold and J. Burgdörfer, J. Phys. B **26**, 3101 (1993).
[21] R. Abrines and I. C. Percival, Proc. Phys. Soc. London **88**, 861 (1966).
[22] J. Burgdörfer, and J. Gibbons, Phys. Rev. A **42**, 1206 (1990); J. Burgdörfer, in *High Energy Ion-Atom Collisions*, edited by D. Berényi and G. Hock, Lecture Notes in Physics Vol. 294 (Springer, Berlin, 1988), p. 344; in *High Energy Ion-Atom Collisions*, edited by D. Berényi and G. Hock, Lecture Notes in Physics Vol. 376 (Springer, Berlin, 1990), p. 199; C. O. Reinhold, J. Burgdörfer, J. Kemmler, and P. Koschar, Phys. Rev. A **45**, R2655 (1992).
[23] C. O. Reinhold, J. Burgdörfer, K. Kimura, and M. Mannami, Phys. Rev. Lett. **73**, 2508 (1994).
[24] K. Kimura, T. Kishi, and M. Mannami, Nucl. Instrum. Methods B **90**, 282 (1994).
[25] K. Kimura, M. Hasegawa, and M. Mannami, Phys. Rev. A **36**, 7 (1987).
[26] *Semiconductors. Physics of Group IV Elements and III-V Compounds*, edited by K. H. Hellwege *et al.*, Landolt-

Börnstein, New Series, Group III, Vol. 17, Pt. a (Springer-Verlag, Berlin, 1982), p. 398.
[27] I. Torrens, *Interatomic Potentials* (Academic Press, New York, 1972).
[28] J. Burgdörfer, *Review of Fundamental Processes and Applications of Atoms and Ions*, edited by C. D. Lin (World Scientific, Singapore, 1993). pp. 517–615.
[29] P. J. Jennings, R. O. Jones, and M. Weinert, Phys. Rev. B **37**, 6113 (1988).
[30] N. D. Lang and W. Kohn, Phys. Rev. B **3**, 1215 (1971); **7**, 3541 (1973).
[31] R. H. Garvey, C. H. Jackman, and A. E. S. Green, Phys. Rev. A **12**, 1144 (1975).
[32] P. C. Kemeny and M. Cardona, J. Phys. C **9**, 1361 (1976).
[33] F. J. García de Abajo and P. M. Echenique, Phys. Rev. B **46**, 2663 (1992); F. J. García de Abajo, Ph.D. thesis, Universidad del País Vasco, 1993 (unpublished).
[34] H. B. Callen and T. A. Welton, Phys. Rev. **83**, 34 (1951).
[35] P. Nozieres, *Theory of Interacting Fermi Systems* (W. D. Benjamin, New York, 1964).
[36] P. M. Echenique, F. Flores, and R. H. Ritchie, in *Solid State Physics: Advances in Research and Applications*, edited by H. Ehrenreich *et al.* (Academic, New York, 1990), p. 229.
[37] P. M. Echenique, R. Ritchie, N. Barberan, and J. Inkson, Phys. Rev. B **23**, 6486 (1981).
[38] K. Tinschert, A. Müller, G. Hofmann, K. Huber, R. Becker, D. Z. Gregory, and E. Salzborn, J. Phys. B **22**, 531 (1989).
[39] Y. Fujii, S. Fushiwara, K. Narumi, K. Kimura, and M. Mannami, Phys. Rev. A **49**, 1897 (1994); Y. Fujii, Ph.D. thesis, Kyoto University, 1993 (unpublished).
[40] T. F. M. Bonsen and L. Vriens, Physica **47**, 307 (1970); M. E. Rudd, C. A. Sauer, and C. L. Bailey, Phys. Rev. **151**, 20 (1966); D. H. Lee *et al.*, Phys. Rev. A **41**, 4816 (1990).
[41] M. R. C. McDowell and J. P. Coleman, *Introduction to the Theory of Ion-Atom Collisions* (North-Holland, Amsterdam, 1970).
[42] P. Fainstein, V. H. Ponce, and R. Rivarola, J. Phys. B **24**, 3091 (1991).
[43] R. Pfandzelter (private communication); T. Berner, Diploma thesis, Humboldt Universität, Berlin (unpublished); A. Hegmann *et al.*, Europhys. Lett. **26**, 383 (1994).
[44] R. A. Sparrow, R. E. Olson, and D. Schneider, J. Phys. B **28**, 3427 (1995).
[45] K. Kimura (private communication).
[46] J. M. Pitarke, A. Bergara, and R. H. Ritchie, Nucl. Instrum. Methods B **99**, 187 (1995).
[47] J. M. Pitarke, R. H. Ritchie, and P. M. Echenique, Phys. Rev. B **43**, 62 (1991).
[48] C. R. Vane *et al.*, Nucl. Instrum. Methods B **67**, 256 (1992).
[49] C. Froese-Fischer, Comput. Phys. Commun. **43**, 355 (1987).